

Numerical model of water flow in a fractured basalt vadose zone: Box Canyon site, Idaho

Christine Doughty

Earth Sciences Division, E. O. Lawrence Berkeley National Laboratory, University of California, Berkeley

Abstract. A numerical model of a fractured basalt vadose zone has been developed on the basis of the conceptual model described by *Faybishenko et al.* [this issue]. The model has been used to simulate a ponded infiltration test in order to investigate infiltration through partially saturated fractured basalt. A key question addressed is how the fracture pattern geometry and fracture connectivity within a single basalt flow of the Snake River Plain basalt affect water infiltration. The two-dimensional numerical model extends from the ground surface to a perched water body 20 m below and uses an unconventional quasi-deterministic approach with explicit but highly simplified representation of major fractures and other important hydrogeologic features. The model adequately reproduces the majority of the field observation and provides insights into the infiltration process that cannot be obtained by data collection alone, demonstrating its value as a component of field studies.

1. Introduction

Faybishenko et al. [this issue] describe a conceptual model for flow and transport through the fractured basalt vadose zone at the Box Canyon site in southeastern Idaho, including a detailed description of the lithological components of the system. The present paper describes the development of a numerical model based on this conceptual model and its application to a ponded infiltration test. The objectives of the numerical modeling are to aid in experimental design and interpretation and to assess the adequacy of the conceptual and numerical models to capture the salient features of infiltration through a fractured basalt vadose zone.

One of the key issues addressed by the Box Canyon studies is how fracture pattern characteristics and connectivity affect the pattern of water infiltration. For example, does flow occur predominantly through fractures or is matrix flow significant? Is vertical connectivity great enough to allow purely vertical infiltration with little lateral spreading, or does extensive spreading occur? Does entrapped air develop? Given the complex structure of the fracture pattern [*Faybishenko et al.*, this issue, Plate 1 and Figure 5], the choice of how to incorporate fractures in the numerical model has great bearing on whether the numerical model can be a useful tool.

In general, how fractures are incorporated in numerical models depends on the relationship between the scale of the fractures and the scale of the model. For models of laboratory and field experiments focused on individual fractures, explicit representation of the fracture including aperture variation may be desirable. *Doughty* [1995] simulated a two-phase flow experiment through a 7 cm by 7 cm transparent fracture replica, with the aperture distribution (measured by light attenuation) deterministically represented in the two-dimensional model by using the cubic law to relate aperture to permeability. *Salve et al.* [1988, section 3.4] modeled underground seepage experiments in which water was released in a horizontal borehole and

captured in an excavation 2 m below. The three-dimensional model consisted of a single unsaturated fracture and the surrounding rock matrix and used a stochastic representation of permeability variation over the fracture plane.

At a larger scale, interactions between fractures may be more important than variability within individual fractures. *Salve et al.* [1998, section 3.3] modeled an underground seepage experiment through a 2 m by 3 m by 4 m block of rock adjacent to a tunnel wall. The three-dimensional model contained 17 fractures, which were located deterministically based on projections from fracture maps of the tunnel wall and ceiling. Permeability variation within fractures was not considered, except at fracture intersections.

At still larger scales, where many fractures are known to exist but cannot be mapped with certainty, fractures are generally incorporated stochastically [e.g., *Sawada et al.*, 1999] or not represented explicitly at all. In the latter case, studies of flow and transport through partially saturated fractured rock have used stochastic continuum models [e.g., *Birkholzer et al.*, 1999], effective continuum models [e.g., *Pruess et al.*, 1990b], and dual-continuum models [e.g., *Doughty*, 1999a] to account for fractures in an average way.

An excellent overview of techniques for incorporating fractures in numerical flow and transport models is presented by *National Research Council Committee on Fracture Characterization and Fluid Flow* [1996]. The primary emphasis is on saturated conditions, but issues concerning multiphase flow are included as well.

For the present study, the experimental scale (nominally delimited by the 7 m by 8 m infiltration pond and a 20-m-thick section of the vadose zone) incorporates many individual fractures. Even with a dense array of boreholes [*Faybishenko et al.*, this issue, Plate 2a], fractures cannot be mapped accurately enough to be represented deterministically. On the other hand, the highly structured, far from random, nature of the fracture pattern does not lend itself well to stochastic representation. Furthermore, with fracture spacing as large as 5 m the experimental scale is too small for an averaged continuum model to provide much useful information. Therefore the present study

Copyright 2000 by the American Geophysical Union.

Paper number 2000WR900146.
0043-1397/00/2000WR900146\$09.00

uses an unconventional quasi-deterministic modeling approach to represent the fractures. The goal is to incorporate as much information as possible from the conceptual model, which is based not only on the present-day appearance of the fracture pattern but an understanding of how the fracture pattern developed.

As is commonly the case in subsurface hydrology, the complexity of the conceptual model necessitates drastic simplifications to produce a tractable numerical model. Hence numerical results cannot be assumed to be correct from first principles but must prove their value by comparing reasonably to field behavior.

2. Model Development

The numerical simulator TOUGH2 [Pruess, 1987, 1991] simulates two-phase flow of air and water in gaseous and liquid phases together with tracer and heat transport through porous or fractured geologic media, which may be strongly heterogeneous. Darcy's law governs fluid flow through both the fractures and rock matrix, with relative permeability and capillary pressure functions used to describe the interactions between liquid and gas phases. Appendix A presents the governing equations for flow and transport as formulated in TOUGH2.

TOUGH2 has been widely used in the research community and consulting industry for a wide range of problems including environmental remediation, geothermal and petroleum reservoir engineering, and nuclear waste isolation [Pruess, 1995, 1998]. Its ability to model two-phase flow in fractured rock is supported by verification with analytical solutions, comparison to laboratory and field data, benchmarking against other codes, and systematic studies of numerical behavior [Pruess, 1987, 1991; Pruess *et al.*, 1990a, b; Moridis and Pruess, 1992, 1995; Doughty, 1999a]. Of particular relevance for the present problem are verification with a semianalytical solution for one-dimensional infiltration [Philip, 1955; Pruess, 1987], validation to a two-dimensional laboratory infiltration experiment [Vauclin *et al.*, 1979; Moridis and Pruess, 1992], and comparisons of conceptual and numerical approaches for modeling flow and transport in unsaturated fractured rock [Pruess *et al.*, 1990a, b; Doughty, 1999a].

The model for the Box Canyon ponded infiltration test is a two-dimensional vertical cross section, which extends from the ground surface to a depth of 20 m, the approximate depth of a local perched water body. The model domain is uniformly discretized into 0.5 m by 0.5 m square grid blocks, with grid block properties assigned according to the conceptual model of Faybishenko *et al.* [this issue]. Specifically, the modeled domain is composed of an upper basalt flow finger, an underlying rubble zone, and the upper portion of a lower basalt flow finger. Figure 1a shows a plan view of the Box Canyon field site, with the location of the model identified. The model is aligned with the row of slanted boreholes called the S holes. It underlies the NE-SW diagonal (10 m length) of the infiltration pond and extends 5 m beyond the pond on both sides. This cross section makes optimal use of the amount of geologic information available from boreholes. Figure 1b shows a schematic cross section that is approximately aligned with the model, identifying the principal hydrogeological components of the upper basalt flow finger, developed from logs and cores taken from the vertical and slanted boreholes (for a detailed description of these components, see Faybishenko *et al.* [this issue]). Other boreholes not aligned with this cross section

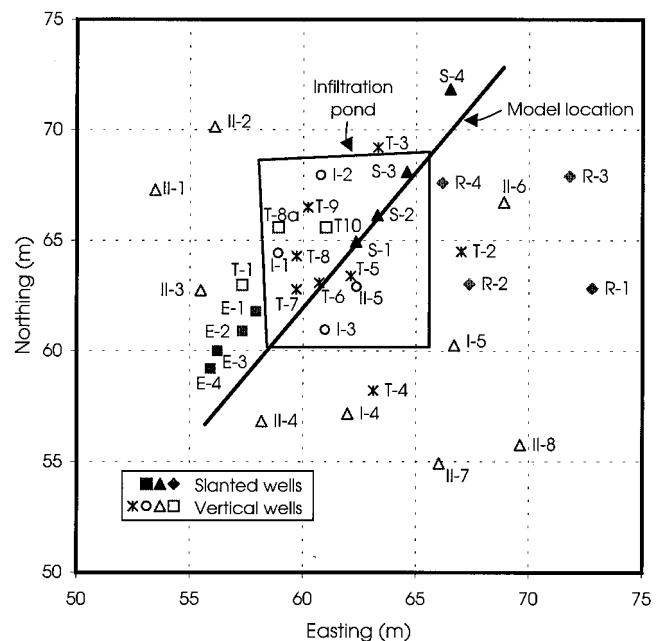


Figure 1a. The Box Canyon field site. Plan view showing the surface trace of the vertical cross-sectional model used for the ponded infiltration test.

show qualitatively similar lithologies, suggesting that the upper basalt flow underlies the entire test site.

The numerical model, shown in Plate 1, includes explicit representation of the following features of the geological model shown in Figure 1b: (1) lens-shaped vesicular zones between depths of 0 and 6 m, (2) a central horizontal fracture zone at a depth of ~ 7 m, (3) nonvesicular massive basalt between depths of 7 and 10 m, (4) vesicular zones at the upper and lower margins of the basalt flow finger, and (5) a rubble zone at a depth of ~ 11 m. Material properties for these components of the model are given in Table 1.

Below the top of the rubble zone, the model becomes much less detailed, as fewer wells are available to constrain the lithology. The lithological log of well II-5 [Long *et al.*, 1995] indicates that the 3–4 m thick region of the model identified as the rubble zone actually consists of four rubble zones, each <0.3 m thick, separated by mostly vesicular, highly fractured basalt. These zones are combined for the numerical model on the basis of results of a hot air injection test [Long *et al.*, 1995], which showed that when hot air was injected at and just above the top of the rubble zone in well S-3, temperature increases in well II-5 were uniformly large over depths of 11–15 m and decreased rapidly beyond those depths. Numerical modeling results [Long *et al.*, 1995] suggest that such persistent temperature changes only arise when large, continuous gas-phase flow paths exist, allowing hot air to move in large quantities. Otherwise, the large heat capacities of rock and water compared to that of air cause the hot injected air to cool rapidly as it flows along small, isolated flow paths surrounded by cold, wet rock.

Fracture pattern is particularly difficult to infer from borehole measurements, and the simple vertical fracture pattern shown in Figure 1b is not believed to be realistic and is thus not used in the model. Instead, the model incorporates the pattern of column-bounding and column-normal fractures observed in the upper basalt flow exposed on the Box Canyon cliff face [Faybishenko *et al.*, this issue, Plate 1]. A 20-m-wide section of

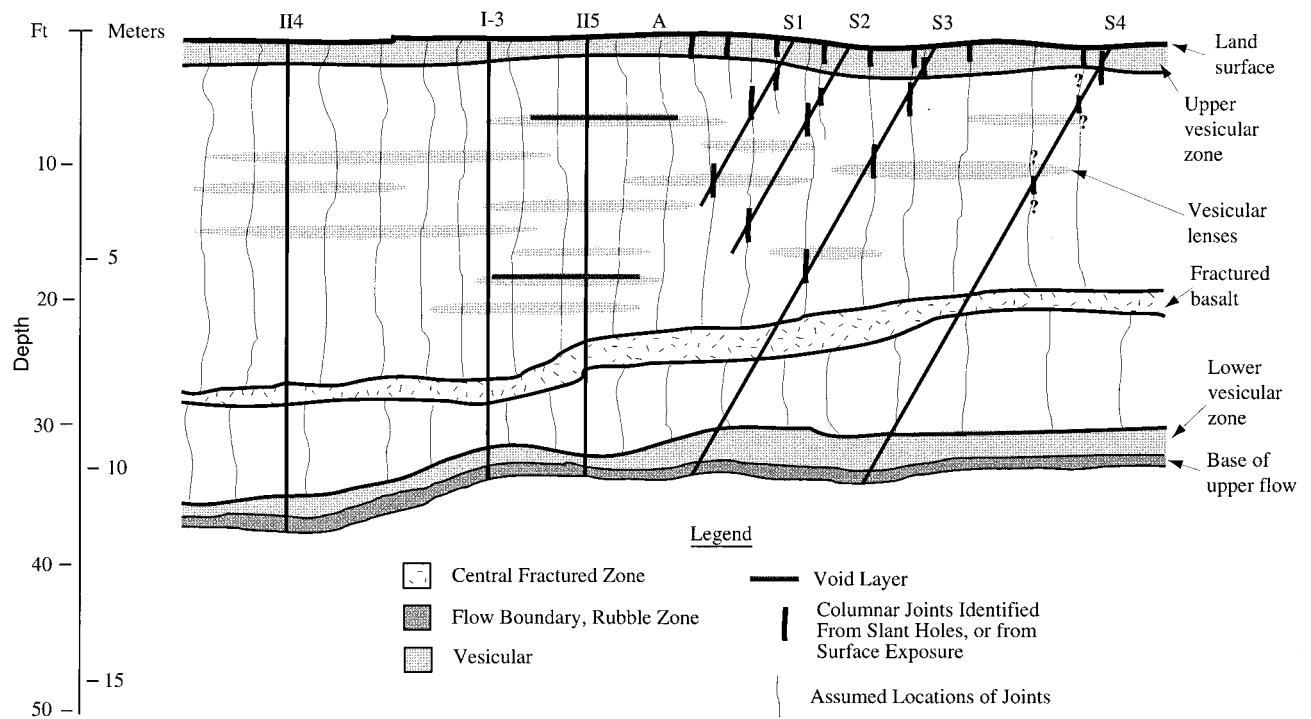


Figure 1b. Vertical cross section through the field site, showing the upper of the two basalt flows modeled and the underlying rubble zone. Note that owing to a lateral jog in the cross section at the point A, well II-5 is not as far from the S boreholes as it appears.

the fracture map of the basalt flow is superimposed on the TOUGH2 grid, and grid blocks underlying fracture traces are denoted fracture grid blocks. Of course, actual fractures are generally much narrower than the half-meter width of the grid blocks, so fracture grid blocks are assigned effective properties that represent a volume of rock matrix containing a fracture. For a vertical fracture the grid block is assigned a large vertical permeability to account for flow through the fracture, a small horizontal permeability to limit fracture/matrix flow, and a small porosity to account for the small aperture of the fracture. For a horizontal fracture the permeability assignment is reversed. Once these assignments have been made, no special treatment is required to model flow between adjacent fracture grid blocks or flow from fracture grid blocks to matrix grid blocks. Flow between any adjacent grid blocks depends merely on the properties of the grid blocks and their vertical position relative to one another.

Soil infilling in shallow fractures that is observed in boreholes and at the ground surface is included in the model by assigning soil properties to near-surface fracture grid blocks. To assign properties for deeper fracture grid blocks, the tree structure developed to categorize the fractures [Faybishenko *et al.*, this issue, Figure 5] is used. Here the column-bounding fractures that extend all the way through the basalt flow finger are denoted primary vertical fractures, shorter column-bounding fractures are secondary vertical fractures, the column-normal fractures connecting primary vertical fractures are primary horizontal fractures, and so on. Permeability and porosity values are assigned to the fracture grid blocks according to this structure, using the assumption that permeability and porosity increase as fracture length increases. Consequently, these properties (Table 1) are highly uncertain, essen-

tially initial guesses to be confirmed or improved by comparing model predictions to observed data.

While the general structure of the fracture pattern mapped at the Box Canyon cliff face is believed to represent the fracture pattern underlying the infiltration pond correctly, specific locations for individual fractures are not likely to be correct. This is because the distance from the cliff face to the infiltration pond is ~ 30 m, whereas the maximum extent of fractures perpendicular to the cliff face is probably < 5 m (the maximum observed fracture spacing along the cliff face is ~ 5 m and the fracture pattern is expected to be isotropic in plan view). Therefore the model is described as a quasi-deterministic model, and it is acknowledged that it cannot make detailed predictions for individual point observations. It can, however, be used to predict behavior at "generic" locations, for example the time dependence of wetting for a location adjacent to a primary vertical fracture. The model can also be used to study the effect of different parameters and processes on the spatial variability of the infiltration process.

Although the model is finely enough discretized to identify individual grid blocks as either representing fracture or matrix (grid block dimension is 0.5 m, with fracture spacing ranging from 0.5 to 5 m), it cannot account for fracture variability within the 0.5-m grid block width. Thus the model does not allow a rigorous treatment of flow within a fracture in which apertures may range from microns to millimeters. A grid refinement exercise for a similar fracture network representation of unsaturated flow [Salve *et al.*, 1998, section 3.3] has shown that halving the grid spacing improves resolution of closely spaced fractures and fracture intersections but it does not alter the overall response of the model in terms of lateral spreading,

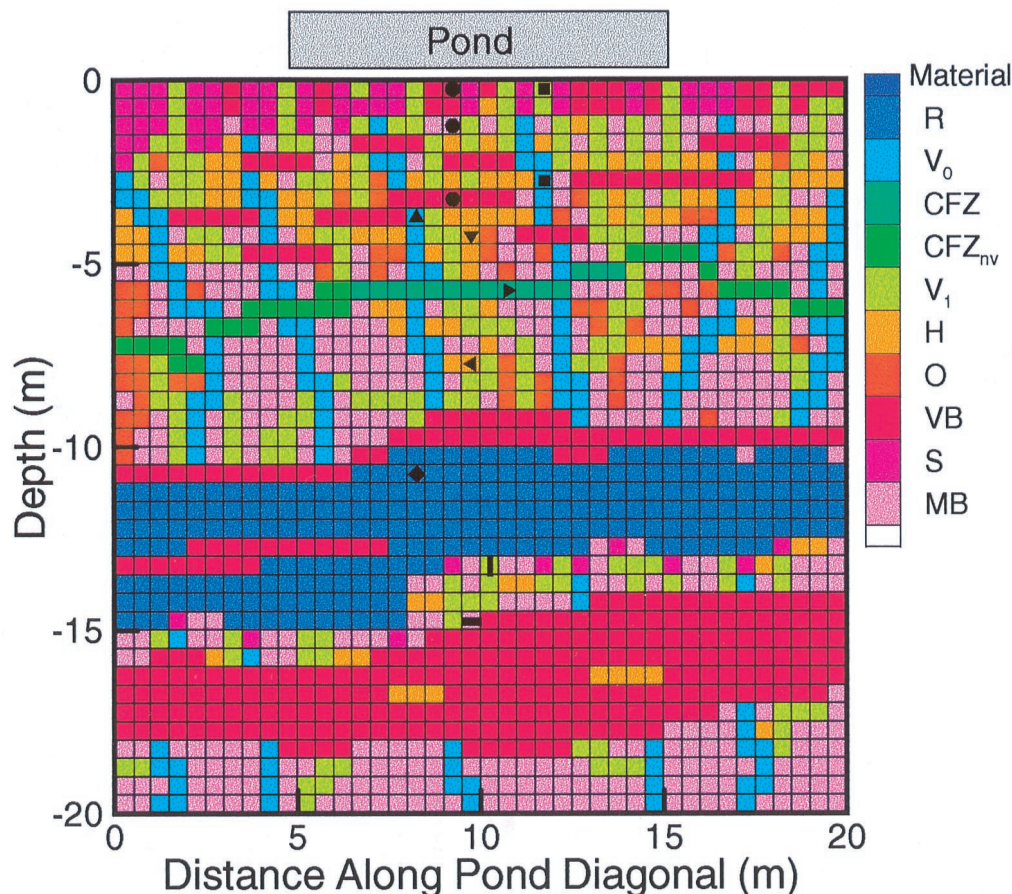


Plate 1. Two-dimensional vertical cross-sectional model used for simulating the ponded infiltration test. Material names and properties are given in Table 1. Locations at which transient model responses are shown in Figures 5 and 9 are identified with black symbols.

fastest transit time through the network, or fracture/matrix flow.

The present use of a coarse grid to represent fracture/matrix interactions is comparable to the traditional dual-porosity ap-

proach [Barenblatt *et al.*, 1960; Warren and Root, 1963]. This approach is widely used to represent fractured media, but it has been shown to produce erroneous results for some transient processes [Doughty, 1999a], and more rigorous treat-

Table 1. Material Properties Used for the Numerical Simulations of the 1996 Ponded Infiltration Test^a

Material Name	Porosity	Permeability, 10^{-15} m^2		Capillary Pressure Strength for Posttest Calculations, Pa
		Horizontal	Vertical	
Rubble zone <i>R</i>	0.50	1,000,000 ^b	1,000,000 ^b	24
Primary vertical fracture <i>V</i> ₀	0.08	50	5,000	230
Central fracture zone				
Vesicular CFZ	0.15	5,000	50	1270
Nonvesicular CFZ _{nv}	0.10	5,000	50	1270
Secondary vertical fracture <i>V</i> ₁	0.07	0.05	500 ^c	850
Horizontal fracture <i>H</i>	0.05	5,000	0.05	1800
Other fracture <i>O</i>	0.05	50	50	1800
Vesicular basalt <i>VB</i>	0.20 ^d	1,000 ^d	1,000 ^d	610
Soil <i>S</i>	0.50 ^e	78 ^e	78 ^e	2,040
Massive basalt <i>MB</i>	0.05	0.05 ^e	0.05 ^e	39,500

^aFracture properties are effective properties of grid blocks containing fractures and surrounding matrix, with permeability and porosity values estimated using tree fracture structure of Faybishenko *et al.* [this issue, Figure 5], unless otherwise noted. Pretest calculations use Corey's [1954] relative permeability functions with $S_{lr} = 0.12$ and zero capillary pressure. Posttest calculations use power law relative permeability functions with an exponent of $n = 5$ and $S_{lr} = 0.1$; and van Genuchten's [1980] capillary pressure with $m = 0.3$ and capillary pressure strength ($1/\alpha$) inferred by calibration to natural state data assuming a background infiltration rate of 10 cm/yr.

^bEstimated from air-injection test data [Long *et al.*, 1995].

^cKnutson *et al.* [1992] and Magnuson [1995].

^dBishop [1991].

^eBaca *et al.* [1992].

ments involving finer matrix discretization are currently under development. Specifically, the lack of fine resolution in the matrix grid blocks means that fracture/matrix flow is likely to be underestimated, which can lead to artificially high fracture flow. A simplified Box Canyon submodel including just one primary vertical fracture shows that when massive basalt surrounds the fracture, using a fine matrix grid does not alter the rate or pattern of liquid flow significantly. On the other hand, when a higher-permeability material such as vesicular basalt surrounds the fracture, fracture/matrix flow is larger with a fine matrix grid, so water propagates more slowly through the fractures. The coarse-grid error accumulates with depth and implies that in the full model, at depths of the central fracture zone and greater, saturation changes due to surface ponding occur about a day too soon.

There are problems associated with representing infiltration through a three-dimensional fracture network with a two-dimensional model. In a two-dimensional model an infiltrating plume cannot spread laterally enough, and in general, water becomes trapped more easily because the connectivity of the model is too low. Several practical constraints motivated the choice of a two-dimensional model rather than a three-dimensional model. Computational requirements for running a three-dimensional model of equivalent extent and resolution to the present two-dimensional model, while technically feasible with present computing resources, would become burdensome. Similarly, construction of the two-dimensional model was very time consuming, and using the same procedure for a three-dimensional model would probably not be worthwhile, with so many model parameters poorly constrained. Development of a more automated mesh generator is a possibility for future studies. In the meantime, note that the fracture pattern is generally isotropic in plan view, so omission of the third dimension does not cause any qualitatively different behavior to be lost, and lateral spreading is least significant beneath the center of the infiltration pond, where the model is centered.

3. Model Application

Prior to the 1996 ponded infiltration test [Faybishenko *et al.*, this issue] the model was used to simulate the test to provide baseline predictions against which field observations could be compared in order to assess the capabilities of the model. Additionally, sensitivity studies were performed to investigate the impact of some poorly known hydrologic properties. Because it was unknown a priori if the results of the quasi-deterministic modeling approach would bear any resemblance to field observations, the pretest simulations were kept relatively simple.

As data from the test began to be evaluated, it became apparent that the numerical model did provide useful results but that it would benefit from the inclusion of additional physical processes. Therefore a series of posttest simulations was done, in which additional features were added and certain aspects of the model were calibrated to observed behavior.

3.1. Pretest Calculations

Two alternative approaches are taken during pretest studies. The first is the traditional soil physics approach, in which air is a passive spectator. The second, more rigorous, approach is to consider the fully coupled two-phase flow of water and air. The primary motivation for using the soil physics approach is numerical efficiency. The addition of air to infiltration problems can cause severe numerical difficulties, especially for highly

heterogeneous media, because liquid-phase and gas-phase processes occur on very different timescales. Using the fully coupled two-phase approach allows the development of entrapped air, which is believed to be an important effect for infiltration into heterogeneous media [Faybishenko, 1993, 1995]. Most of the calculations assume isothermal conditions at 10°C.

The model uses Corey [1954] curves (see Appendix A) to describe the dependence of relative permeability on saturation. For these curves the sum of liquid- and gas-phase relative permeabilities is much less than one, implying that there is strong interference between the two fluid phases. This is considered reasonable for flow in fractured media because the flow geometry is generally more restricted than in three-dimensional porous media [Pruess and Tsang, 1990; Persoff and Pruess, 1995]. Capillary forces are neglected in the model, meaning liquid flows primarily in response to gravity. In reality, flow paths and moisture distributions develop in response to a combination of gravity and capillary forces, with gravity acting to localize flow in high-permeability vertical pathways and capillary forces spreading moisture to lower-permeability regions diffusively. Thus the model is expected to show a sharper picture of preferential flow than may actually exist.

The simulation initial condition is a uniformly partially saturated medium with liquid saturation $S_l = 0.1$, in which water is immobile (residual liquid saturation $S_{lr} = 0.12$). For the fully coupled two-phase calculations a gas-static pressure profile is also specified. The pond boundary is represented by a liquid-saturated, constant pressure boundary corresponding to the planned depth of water in the pond (0.3 m). For the fully coupled two-phase calculations a constant pressure boundary representing the atmosphere overlies the nonpond portion of the model upper boundary; otherwise, this is a closed boundary. Lateral and lower boundary conditions are constant saturation and constant pressure boundaries. Lateral boundaries are open to flow, and the lower boundary, which represents a local perched water body, is open to liquid flow.

Figures 2 and 3 show the predicted change in liquid saturation distribution from the initial state and the liquid flow field at a series of times for the soil physics and fully coupled two-phase simulations of the ponded infiltration test, respectively. In both cases the infiltration does not proceed uniformly but follows highly irregular paths, bypassing the massive basalt sections and focusing in the high-permeability fractures. As a result, the tributary structure of the fracture pattern [Faybishenko *et al.*, this issue, Plate 1 and Figure 5] causes a funneling of the infiltrating water, which is particularly apparent below the central fracture zone (6–7 m depth). Several types of field observations made during the ponded infiltration tests support a funneling of flow as depth increases [Faybishenko *et al.*, this issue]. Along with this funneling, a moderate amount of lateral spreading occurs, with the overall plume width increasing from its original 10 m to ~15–18 m near the bottom of the model. The primary avenues for lateral flow are vesicular lenses, the central fracture zone, and the rubble zone.

Figure 4 compares the infiltration rate from the pond with the simulated values. The model reproduces the general trend of decreasing infiltration rate, but the simulations show a smaller overall decrease in infiltration rate than is observed in the field. Sensitivity studies described below indicate that by varying flow parameters the modeled infiltration rate curve can be shifted up or down but the shape of the curve never changes enough to match the observed curve closely. This discrepancy could indicate a fundamental shortcoming of the model. However, it is also possible that an early time underprediction of

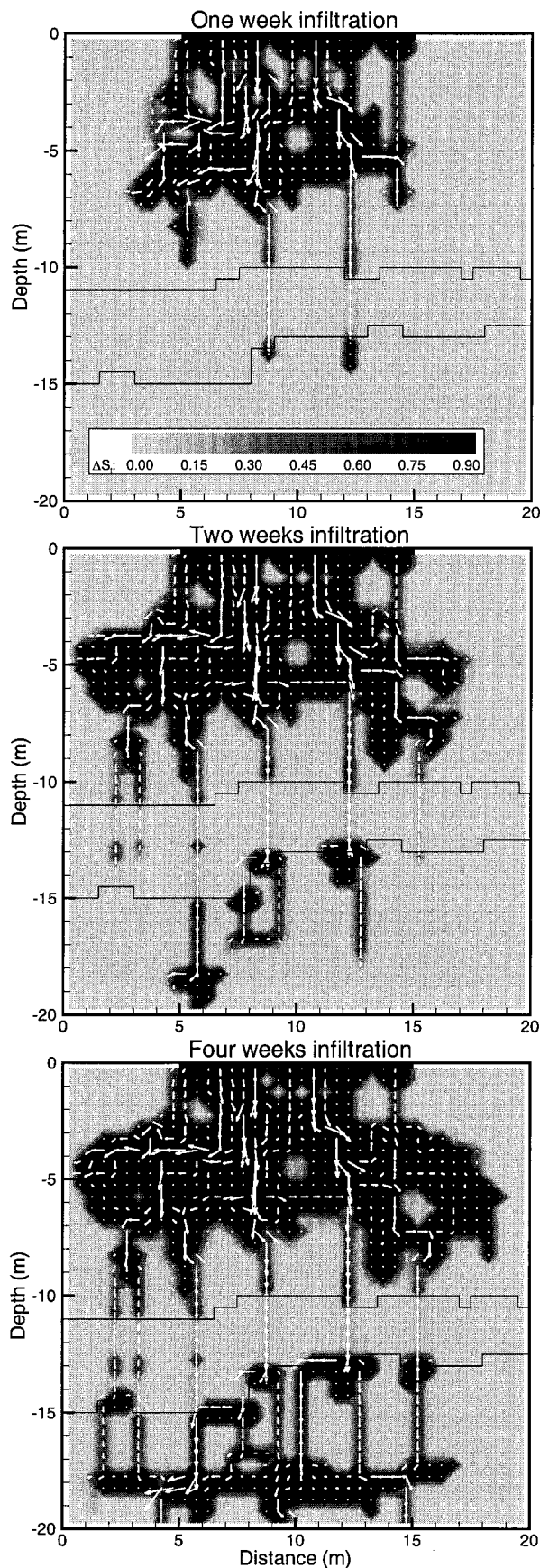


Figure 2. Simulated change in liquid saturation from the initial state ($S_l = 0.1$) and liquid flow field at a series of times during the infiltration test for the soil physics pretest calculation. The infiltration pond and rubble zone boundaries are also shown.

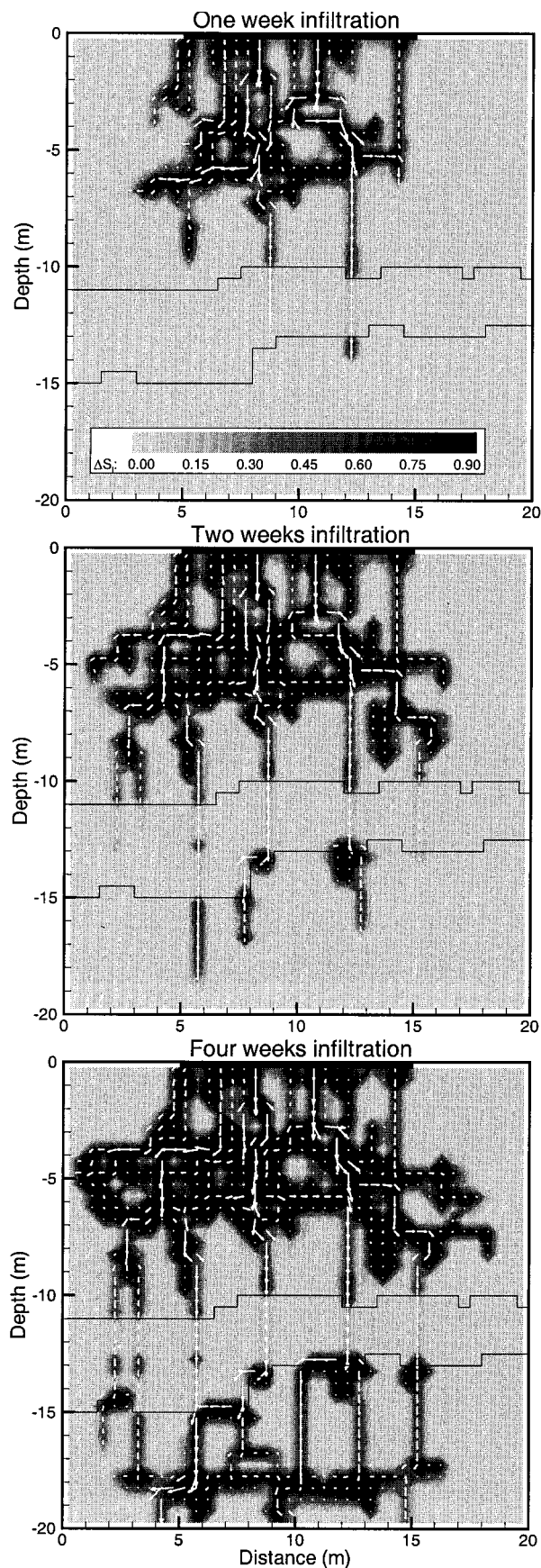


Figure 3. Simulated change in liquid saturation from the initial state ($S_l = 0.1$) and liquid flow field at a series of times during the infiltration test for the fully coupled two-phase pretest calculation.

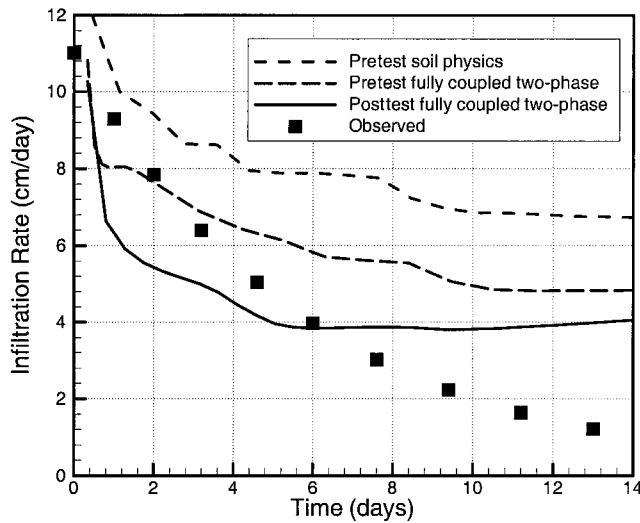


Figure 4. Comparison of simulated and observed infiltration rates for the pretest and posttest calculations.

infiltration rate by the model arises because of leaks that existed in the pond during the first few days of the test, resulting in a larger area available for infiltration than in the model. Furthermore, the late time overprediction of infiltration rate by the model may be the result of decreased permeability caused by clogging of flow paths by fine materials, another process believed to be occurring in the field that is not included in the model.

The fully coupled two-phase simulation yields significantly different results than does the soil physics simulation, suggesting that entrapped air plays an important role and should be included in the model. Although the infiltrating water generally finds the same preferential pathways for the both cases (compare Figures 2 and 3), more regions are bypassed by liquid water, making the saturation distribution much less uniform, when entrapped air develops. Subsurface flow rates are also smaller due to the enhanced flow resistance caused by pressure buildups due to entrapped air. The total infiltration rate from the pond is therefore smaller as well (Figure 4).

Figure 5 compares the transient response to ponding at selected locations in the model to observed values in wells T-5 and T-9. The model locations cannot be exactly identified with wells T-5 and T-9 because the model is not that precisely defined (recall that the fracture pattern is taken from the cliff face exposure 30 m away), and in any event, wells T-5 and T-9 are offset from the pond diagonal with which the model is aligned (Figure 1a). The model observation locations (shown in Plate 1) were chosen to match the lithology observed in wells T-5 and T-9 at the depths of the sensors in order to illustrate representative model results. The observed data show capillary pressure P_c , which is not included in the model, so liquid saturation S_l is plotted instead. Without assuming an explicit form for $P_c(S_l)$ a quantitative comparison of modeled and observed results is not possible, but a qualitative comparison can be made merely by assuming that $P_c(S_l)$ is a continuous function.

Prior to the start of ponding, all observed pressures are negative, indicating unsaturated conditions prevail. At the 0.3-m depth in both wells, where lithological logs [Faybishenko *et al.*, 1998] indicate that moderately permeable vesicular ba-

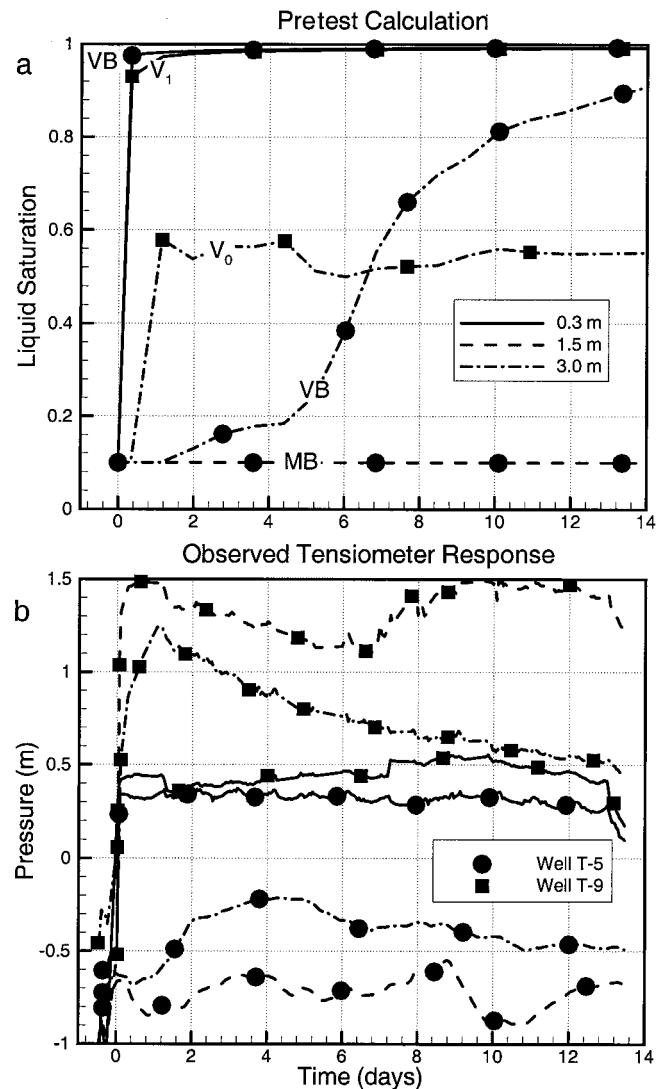


Figure 5. Comparison of (a) simulated and (b) observed transient responses to ponded infiltration at locations representing wells T-5 and T-9 (circles and squares, respectively, in Plate 1) for the fully coupled two-phase pretest calculation. The model material in which each response occurs is also shown in Figure 5a.

salt is found, the observed data show a rapid pressure increase when ponding begins, followed by a steady positive pressure, indicating a rapid transition to saturated conditions. The corresponding modeled responses also show a rapid increase to steady near-saturated conditions. There is no observed or modeled response at the 1.5-m depth in well T-5, where low-permeability massive basalt is apparently bypassed by the flow. The small, gradual pressure increase observed in well T-5 at 3 m occurs in vesicular basalt and is well matched by the slow saturation increase in the model. There is a strong, oscillating pressure response observed in well T-9 at 1.5 m, where the lithological log identifies a fracture. A response with similar characteristics is seen in the model in a primary vertical fracture at the 3-m depth. The oscillations likely occur as the downward moving plume encounters large changes in permeability, arising from openings or constrictions in fracture flow paths. The pressure response observed in well T-9 at 3 m also

Table 2. Sensitivity Studies Conducted Prior to the 1996 Ponded Infiltration Test

Case	Two-Phase Flow Approach	Features	Infiltration Rate, ^a cm/d
13	soil physics	base case with no entrapped air	6.6
16	fully coupled	base case with entrapped air	4.9
17	fully coupled	air more mobile (<i>van Genuchten's</i> [1980] relative permeabilities with $k_{rg} = 1 - k_{rl}$)	5.8
26	fully coupled	air and water more mobile (linear relative permeabilities)	5.8
19	soil physics	fracture porosities decreased by about a factor of 10	6.5
20	soil physics	fracture permeabilities increased by a factor of 10	30.5
18	soil physics	fractures do not go to ground surface	4.3
24	fully coupled	fractures soil-filled below rubble zone	4.9
25	fully coupled	fractures replaced by massive basalt below rubble zone	4.9
22	fully coupled	nonisothermal case, pond water is 20°C, initial subsurface temperature is 10°C	6.4

^aAfter 21 days of ponded infiltration, infiltration rate is approximately steady.

suggests a fracture in which a steady flow regime does not develop. After a large, early pressure response indicating rapid water arrival the gradual pressure decline suggests that the fracture begins to drain and hence does not remain part of the main network of preferential flow channels. This type of behavior is not observed in the model, but overall, the model captures most of the different kinds of transient behavior observed in the field.

Table 2 summarizes the sensitivity studies conducted and shows the predicted infiltration rate from the pond for each one. Parameters studied include fracture transmissivity and effective porosity, the vertical extent of fractures near the ground surface and below the rubble zone, and the relative permeability functions used. The infiltration rate ranges from 5 to 33 cm/d, depending primarily on the transmissivity assumed for the largest vertical fractures. The shapes of the infiltration rate curves are all similar to those for the base case simulations, shown in Figure 4.

When air relative permeability is increased (case 17) or the interference between liquid and gas phases is lessened (case 26), the effect of entrapped air decreases and infiltration rate increases. The values of infiltration rate intermediate between cases 13 (no air entrapment) and 16 (full air entrapment) are reasonable for these partial air entrapping conditions.

If fractures do not extend to the ground surface (case 18 compared to case 13), the infiltration rate from the pond decreases significantly. A decrease in fracture porosity (case 19 compared to case 13) does not affect infiltration rate but does shorten the arrival times of the water at various depths in the model. Increasing fracture permeability by a factor of 10 (case 20 compared to case 13) greatly increases infiltration rate, well beyond the observed values, providing constraints on the range of actual fracture permeabilities.

The lack of widespread lateral flow at the base of the rubble zone is somewhat surprising, given results of a large-scale infiltration test conducted by the Idaho National Engineering and Environmental Laboratory in 1994 at a site several kilometers away from Box Canyon. In that test, lateral flow in a rubble zone overlying a sedimentary interbed persisted for at least 100 m [Wood and Norrell, 1996]. Two variations in the Box Canyon model were considered. In the first (case 24), permeability just below the rubble zone was decreased by converting fracture grid blocks to soil-filled fracture grid blocks, which results in about a factor of 10 decrease in the highest permeabilities underlying the rubble zone. This change has almost no

effect on the model results. In the second variation (case 25) all grid blocks underlying the rubble zone were converted to massive basalt, resulting in the complete cessation of vertical flow beneath the rubble zone. Rather than reaching the perched water body, infiltrating water is diverted laterally along the base of the rubble zone and exits the model through a lateral boundary. This study suggests that the permeability of the sedimentary interbed noted in the 1994 test must be very low and that the interbed must be continuous for such widespread lateral flow to occur.

A nonisothermal calculation (case 22), in which the pond water is maintained at 20°C (due to solar heating), produces saturation distributions that differ from the base case (case 16) only slightly but results in a 30% higher infiltration rate because of the temperature dependence of the viscosity of water, $\mu(T)$ ($\mu(20)/\mu(10) = 1.3$).

3.2. Posttest Calculations

During the ponded infiltration test, gas bubbles were observed in the pond, indicating that air can become entrapped (and subsequently released) beneath the pond, rather than simply being purged by the infiltrating water. Therefore the model considers the fully coupled two-phase flow of water and air. Because temperature effects were shown to be minor in the pretest sensitivity study, isothermal conditions are assumed. To improve on the realism of the modeled saturation distribution, nonzero capillary pressures and background (natural state) infiltration are included. This represents a significant additional complexity compared to the pretest calculations, which did not attempt to develop realistic natural state conditions.

The capillary pressure strength of each material and the average background infiltration rate are determined by calibrating the natural state conditions predicted by the model to estimates of capillary pressure and saturation made prior to the ponded infiltration test. The average background infiltration rate is implemented as a liquid water source term in each of the uppermost active (i.e., nonboundary) grid blocks of the model, which have a large horizontal permeability to allow the water to laterally redistribute and infiltrate nonuniformly through the model. After several natural state simulations, using capillary pressure strengths and background infiltration rate chosen by trial and error, the parameter set given in Table 1 and a background infiltration rate of 0.027 cm/d (10 cm/yr) are obtained. This infiltration rate is somewhat larger than the 1–5 cm/yr used in other vadose zone studies of the Snake River

Plain [Rawson *et al.*, 1989; Magnuson, 1995], but those studies consider sites with thick alluvial fill, where evapotranspiration rates are higher.

The modeled natural state liquid saturation and capillary pressure distributions are shown in Figure 6. All the model capillary pressures are within the observed range (-1 to -3 m), but the liquid saturations tend to be lower than those observed, except in the massive basalts just above the rubble zone. The rubble zone and primary vertical fractures are believed to be relatively dry under natural conditions, since their high permeabilities are associated with weak capillary pressures, and this is adequately represented by the model. However, the vesicular basalt lenses and shallow soil layer should be wetter (0.7 – 0.8 rather than 0.3 – 0.4). To achieve this and at the same time maintain a reasonable match to the ponded infiltration rate would require introducing different relative permeability functions for different materials and a great deal more fine tuning of parameters. Given the lack of hydrologic data available for the geologic materials at Box Canyon, and the overall simplicity of the numerical model, it is not considered worthwhile to attempt this. Despite its shortcomings, the natural state model portrays a reasonable flow distribution (Figure 6). The primary throughgoing vertical fractures are not the main pathways for background liquid flow in the upper 7 m of the model, as their low liquid saturation makes their relative permeability lower than that of smaller vertical fractures. Instead, flow is widely distributed among all the vertical fractures in this depth range.

Figure 6 also shows the natural state moisture content distribution θ , where $\theta = S_r\phi$, the product of liquid saturation and porosity. Moisture content is the physical variable to which geophysical methods such as neutron logging and ground-penetrating radar are sensitive. Because of the large differences in porosity for the different hydrogeological components at Box Canyon, distributions of liquid saturation and moisture content may look quite different. In particular, the high porosities of the soil and rubble zone convert even small liquid saturations to significant moisture contents. The moisture content distribution shown in Figure 6 is consistent with neutron logging and ground-penetrating radar surveys conducted prior to the infiltration test, which tend to show high moisture contents in the central fracture zone and rubble zone [Faybishenko *et al.*, this issue; Faybishenko *et al.*, 1997; Peterson and Williams, 1997].

The natural state liquid saturation distribution shown in Figure 6 provides the initial conditions for the simulation of the ponded infiltration test. Background infiltration continues throughout the simulation and the constant pressure boundary at the pond is held at 0.23 m, corresponding to the depth of water in the pond. Figure 7 shows the simulated change in liquid saturation from the natural state and the liquid flow field at a series of times during the test. The posttest calculation shows much more gradual, widespread saturation changes than does the pretest calculation (Figure 3), which is consistent with the addition of capillarity. However, the overall pattern of localized, preferential flow through vertical fractures, with lateral spreading through the subhorizontal high-permeability pathways afforded by vesicular lenses, the central fracture zone, and the rubble zone is present for both pretest and posttest calculations, making the overall infiltration patterns similar. Within the rubble zone, vertical flow is much more uniformly distributed than for the pretest calculation, another expected consequence of the addition of capillarity. Note that

in the posttest calculation at $z = 3$ m, $x = 15$ m, enhanced lateral flow in a vesicular zone has made possible a completely new flow path, one that exits the model at a depth of ~ 4 m (compare Figures 3 (top) and 7 (top)). Such large consequences of small changes in flow conditions are to be expected in strongly heterogeneous media, as described by Faybishenko *et al.* [this issue].

Figure 7 shows that as in the pretest calculations, lateral flow along the base of the rubble zone is not continuous over more than a meter or so owing to the presence of underlying vertical fractures that intercept the water. In contrast, perched water was observed in the field at the rubble zone depth in wells up to 5 m away from the infiltration pond [Faybishenko *et al.*, this issue], suggesting that more extensive lateral flow occurs through the rubble zone than is predicted by the numerical model. This in turn requires a greater extent of low-permeability material underlying the rubble zone than is present in the model. Such a layer could exist if fracture spacing beneath the rubble zone were greater than that suggested by the cliff face fracture map or if fractures existed but had lower permeability than indicated by core samples. In any event, such hydrological responses provide valuable means to improve the numerical model, in that they do not require either extrapolation (as do cliff face observations) or interpolation (as do core-scale measurements), both of which are unreliable operations in highly heterogeneous systems.

Figure 8a shows the simulated liquid saturation distribution and the liquid flow field after 2 weeks of ponded infiltration. Showing the saturation distribution itself, rather than the change in saturation from the natural state as in Figure 7, enables the infiltration process to be seen in the same context as by the monitoring instruments in the field. The liquid flow field shows that under ponded boundary conditions the primary vertical fractures provide the main pathways for liquid infiltration, in contrast to the background liquid flow field shown in Figure 6. Figure 8b shows the simulated change in moisture content from the natural state and the gas flow field. The primary differences between the saturation changes (Figure 7) and moisture content changes show up in the soil and rubble zones, where porosity is large. Simulated changes in moisture content are generally consistent with ground-penetrating radar difference tomograms, showing large increases in the soil, central fracture zone, and rubble zone [Faybishenko *et al.*, this issue; Peterson and Williams, 1997]. Despite the strong signature of the column-bounding fractures in the liquid flow field, they do not show up as clearly as moisture content changes, owing to their small porosity, thus making them difficult to image with geophysical methods such as ground penetrating radar. The gas flow field shows that most of the gas is purged from the subsurface during the initial stages of infiltration by lateral flow along high-permeability fractures and through the rubble zone. A few gas flow paths rise vertically within the infiltrating plume; these correspond to the gas bubbles observed in the pond during the infiltration test.

Figure 9 shows the simulated transient liquid saturation and capillary pressure response to ponding at selected locations in the model (identified in Plate 1). As in the pretest simulations, there is a great variety in response, depending not only on the lithology at the monitoring location but on the conditions along the entire pathway from the ground surface to the monitoring point. Similar behavior is observed in the field [Faybishenko *et al.*, this issue].

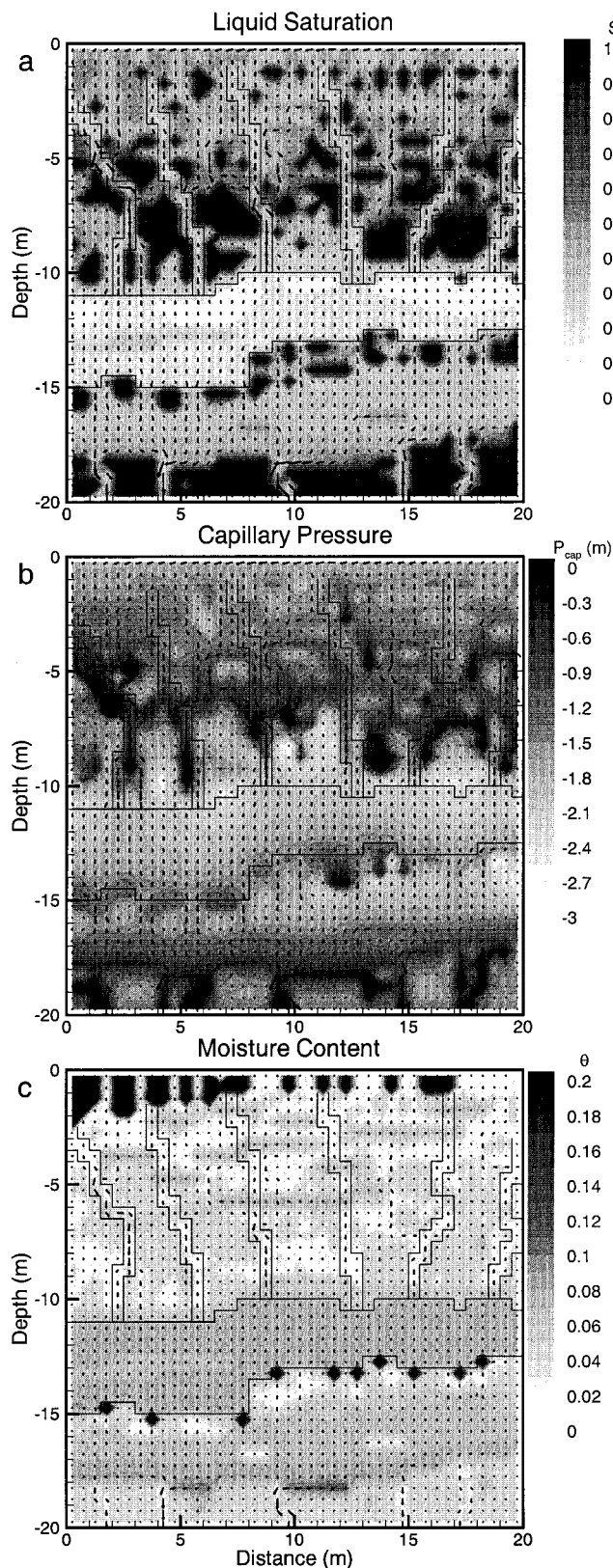


Figure 6. Simulated natural-state distributions of (a) liquid saturation, (b) capillary pressure, and (c) moisture content used as initial conditions for the posttest calculation. Arrows show the liquid flow field. A background infiltration rate of 10 cm/yr is imposed. The locations of the primary vertical fractures above the rubble zone are also shown.

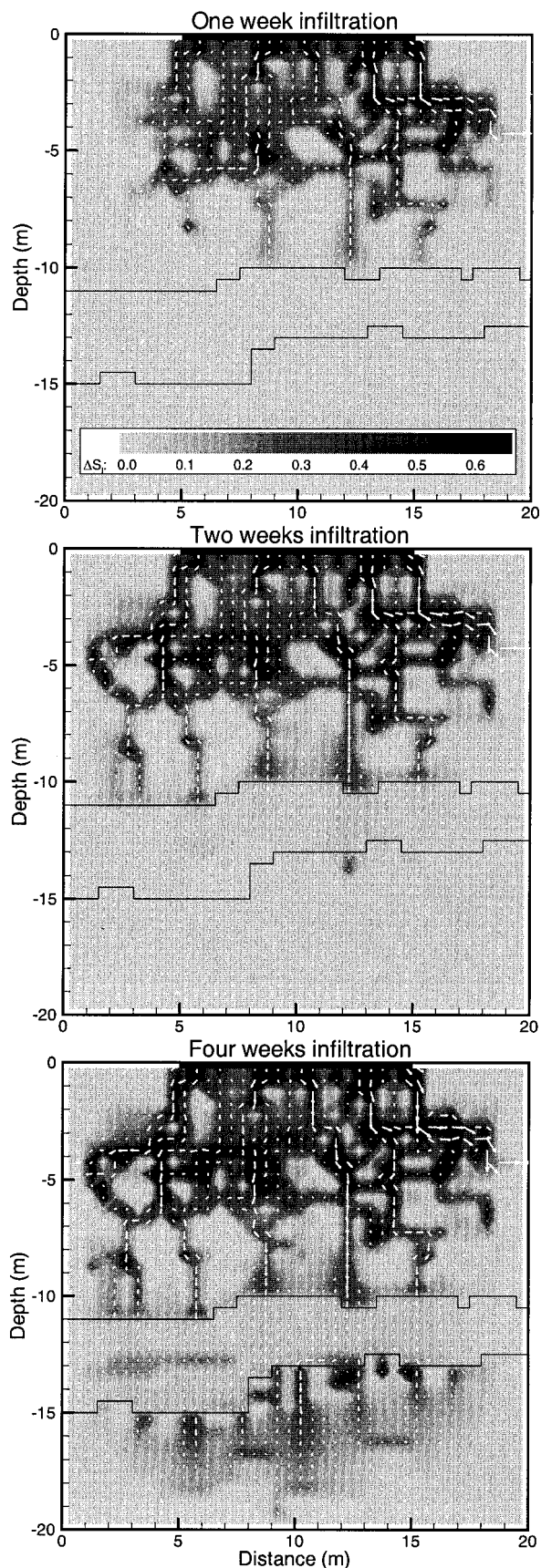


Figure 7. Simulated change in liquid saturation from the natural state (shown in Figure 6a) and liquid flow field at a series of times during the infiltration test for the posttest calculation. Note the change in saturation scale from Figures 2 and 3.

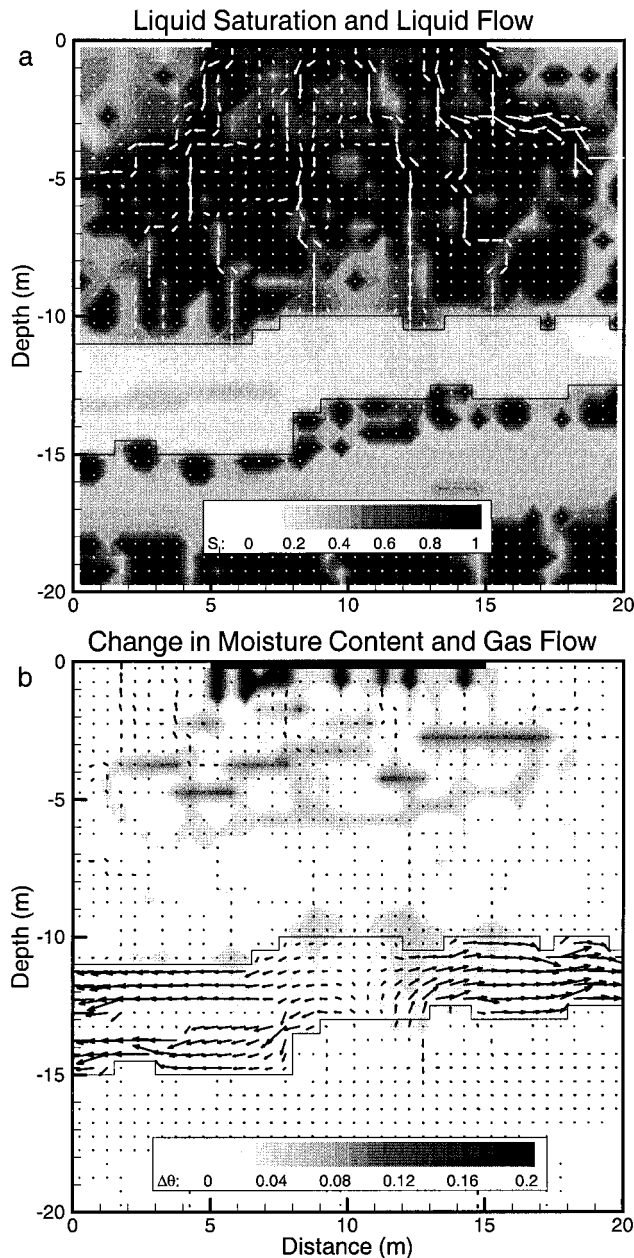


Figure 8. Simulated results after 2 weeks of ponded infiltration for the posttest calculation: (a) liquid saturation and liquid flow field and (b) change in moisture content from the natural state (shown in Figure 6c) and gas flow field.

The infiltration rate from the pond is shown in Figure 4. The overall decreasing trend is similar for the posttest calculation, the pretest calculations, and the observed data. However, the posttest calculation levels off earlier than do the pretest calculations, suggesting an earlier transition to gravity-driven flow. The shorter transient period may be the result of the nonuniform initial saturation distribution (Figure 6), which makes the medium seem less heterogeneous, as the segregation of liquid into rocks with strong capillary pressure tends to decrease the effective permeability of the materials with the highest intrinsic permeability and vice versa.

Although the ponded infiltration test lasted only 2 weeks, it is of interest to examine the long-term response to ponding.

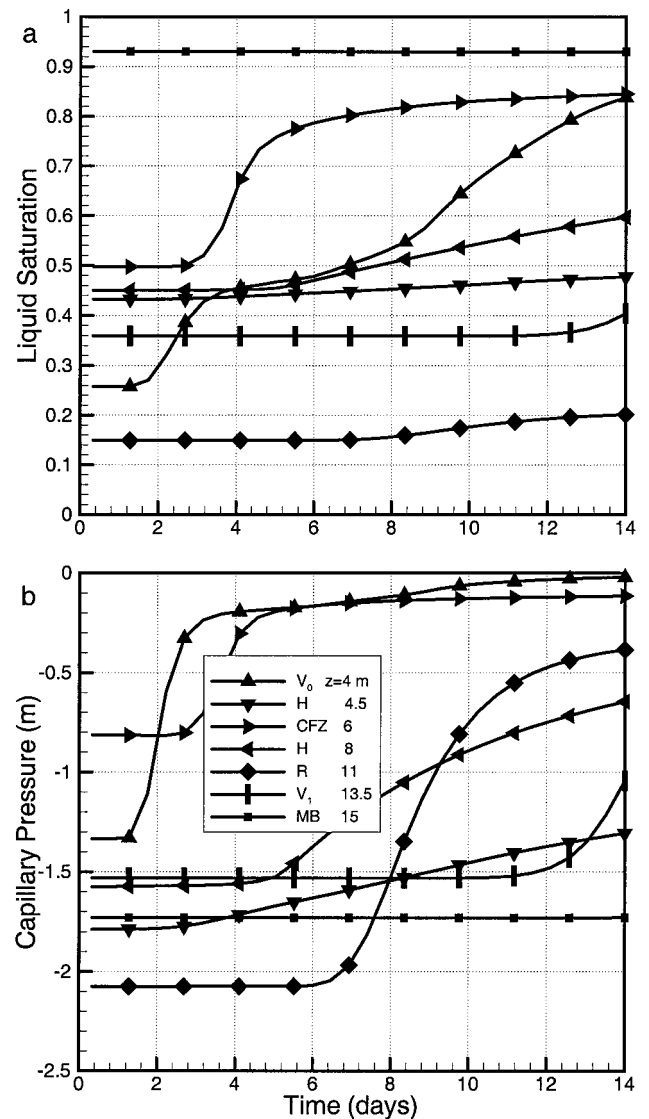


Figure 9. Simulated transient responses of (a) liquid saturation and (b) capillary pressure at selected locations (shown in Plate 1) for the posttest calculation.

Figure 10 shows the infiltration rate from the pond for models using the fully coupled two-phase approach and the soil physics approach. The two cases both show a decreasing infiltration rate at early times, but the infiltration rate for the fully coupled two-phase flow case is smaller than that for the soil physics case owing to entrapped air effects (as in Figure 4). For both cases, infiltration rate decreases until the infiltrating plume reaches the lower constant pressure boundary of the model, at ~ 1 week. At this time, infiltration rate for the soil physics case becomes constant, and the system has essentially reached steady state. In contrast, at this same time the infiltration rate for the fully coupled two-phase case begins to increase owing to the gradual removal of entrapped air and does not reach a steady state until much later, almost 1 year. The flow out the lower boundary of the model, into the perched water body, is also shown in Figure 10. At steady state the difference between infiltration rate from the pond and flow to the perched water body arises from lateral flow out of the model through the central fracture zone and the rubble zone. The long-term be-

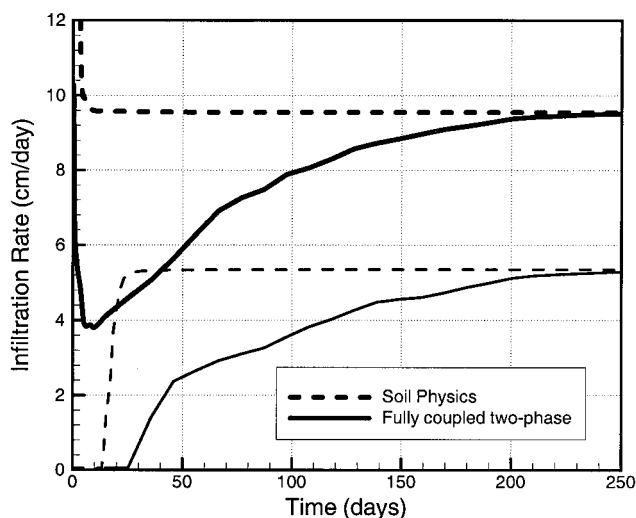


Figure 10. Simulated infiltration rate from the pond for a 1-year-long ponded infiltration test (thick lines) and liquid flow rate out the lower boundary of the model (thin lines).

havior in the field may be rather different from that shown in Figure 10 if part of the observed infiltration rate decrease (Figure 4) arises from a decrease in permeability due to clogging of flow paths by fine particles that were mobilized during the test or by the growth of biofilms. Such a decrease in permeability, which is not included in the numerical model, would lessen or eliminate the late time increase in infiltration rate shown in Figure 10. After 1 year of ponding, the modeled saturation distribution in the highly fractured, upper 7 m of the model is uniformly high, in contrast to the irregular saturation distribution found after 2 weeks of ponding (Figure 8). The primary liquid flow paths remain largely the same, but slower flow from the primary vertical fractures to lower-permeability components of the system results in a more uniform saturation distribution.

It is also of interest to consider the evolution of the liquid saturation distribution and liquid flow field during the drain-out period following a ponded infiltration test. Model results suggest that the drain out proceeds irregularly, just as infiltration does, with the high-permeability pathways draining first. In contrast to the infiltration process, in which large changes in saturation occur at early times, drain out appears to occur more gradually and is slower overall. This difference arises because of the different roles of large fractures, the fastest responding components of the system, during infiltration and drainage. During infiltration the large fractures wet quickly and remain the dominant flow paths throughout infiltration. In contrast, during drain out, these fractures drain quickly and thereafter do not control the drain-out process. The model predicts that the Box Canyon site will return to its undisturbed natural condition after about a year. However, field observations made just prior to the second ponded infiltration test [Faybishenko *et al.*, this issue] indicate that even after 1 year, the site was still quite wet. It is also noteworthy that while the pretest and posttest simulations produce comparable predictions for the evolution of an infiltrating plume, they grossly differ in their predictions of drain out, with pretest simulations predicting that it would take many years to return to undisturbed conditions. These findings suggest that drain out is more sensitive to capillarity than infiltration is and that further parameter adjustments are required to model it properly.

4. Summary and Conclusions

Numerical modeling of the ponded infiltration test conducted at Box Canyon has been conducted in coordination with field activities. Simulations were conducted prior to the test as part of the experimental design process: to study the sensitivity to different conditions and to predict the results of the test. Simulations were conducted after the test to help explain the observed results and to assess the capabilities of the conceptual and numerical models. In general, the iterative sequence of model-test-model has proved useful for gaining an understanding of both the physical processes at work and the strengths and weaknesses of the model's representation of them.

The numerical model uses an unconventional quasi-deterministic approach that includes a highly simplified representation of the key hydrogeologic features of the fractured basalt vadose zone. In particular, the model attempts to maintain fracture network connectivity but omits many smaller-scale details, such as aperture variation within individual fractures and a rigorous treatment of fracture/matrix interactions. The quasi-deterministic model results have been generally consistent with field observations, and modeling has been an effective tool to aid in experiment interpretation. Some specific insights gained from the modeling are presented below.

The pretest simulations, which ignore capillarity, suggest that infiltration does not occur uniformly but follows irregular flow paths through the highest-permeability features. Some lateral spreading occurs through vesicular zones and the central fracture zone, but flow through the rubble zone is nearly vertical. Entrapped air is shown to have a large effect, decreasing infiltration rate and creating a less uniform subsurface saturation distribution.

The posttest simulations add realism to the model by considering stable initial conditions in which gravity and capillary forces are balanced. The overall shape of the infiltrated plume is similar for both pretest and posttest simulations, with the flow distribution controlled by the high-permeability features, suggesting that the greatly simplified pretest simulations are useful for studying infiltration through the highly fractured Snake River Plain basalt. However, by incorporating capillarity the model treats fracture/matrix interactions more accurately and better illustrates how the system response compares to ambient conditions, which must be appreciated to design effective monitoring devices.

A comparison of observed and modeled natural state conditions was used to estimate values of poorly constrained model parameters. Such an inverse analysis would be even more effective if it were expanded to incorporate responses during and after the ponded infiltration test. By optimizing model parameters for both low and high infiltration rates and under wetting and draining conditions, subsequent model predictions could be made with greater confidence.

One of the key questions addressed by the modeling studies is how fracture pattern characteristics and connectivity affect the pattern of water infiltration. Simulations show that strongly preferential gas-phase flow occurs through the subhorizontal rubble zones that exist between basalt flows because the permeability of these zones is several orders of magnitude higher than any other hydrological component at the site. In contrast, widespread lateral liquid flow through the rubble zone only occurs if there are no underlying vertical flow paths because gravity plays such a dominant role in controlling liquid flow. For liquid infiltration from the ground surface the vertical flow

paths with the highest effective permeability are active. At the Box Canyon site, there are no vertical rubble zones near the ground surface, so the next most permeable flow paths, individual fractures and fracture zones, become the key hydrological component. Under background (low infiltration rate) conditions the largest fractures are drained, leaving the highest effective permeability (intrinsic permeability times relative permeability) in the smaller fractures. Under ponded infiltration conditions the largest fractures wet up and provide the primary vertical flow paths. The tributary structure of the fractures causes the liquid flow to undergo a funneling process with depth, which has been indirectly observed in the field [Faybishenko *et al.*, this issue].

A recurring theme of the field observations at Box Canyon is that the local lithology alone is not enough to predict what kind of response will be observed at a given point in the subsurface. Rather, local responses depend on the entire flow path from the surface [Faybishenko *et al.*, this issue]. This finding reinforces the notion that fracture connectivity is of crucial importance in predicting the fate of contaminants migrating downward from the surface with infiltrating water. The quasi-deterministic modeling approach, which is designed to maintain fracture connectivity, has been compared with a more traditional stochastic approach, in which geostatistics is used to construct the permeability distribution as a correlated random field [Doughty, 1999b]. Results suggest that the stochastic approach is less successful in predicting field behavior because too much information about fracture connectivity is lost in the geostatistical analysis. Consequently, the information available to the resulting stochastic model is simply not sufficient to capture field behavior. Of course, there are other means of creating stochastic permeability distributions than through traditional variography. One simple modification involves introducing the concept of a neighborhood into the optimization algorithm used to generate the correlated random permeability field, with acceptance rules that encourage connectivity implemented to augment the objective function based on variograms [Liou *et al.*, 1998]. On the basis of the present study, models that emphasize connectivity over correlation structure are expected to perform better.

Appendix A: Governing Equations for Flow and Transport

The governing equations for fluid and heat flow for a multicomponent system consist of a mass balance for each component m (w for water, t for tracer, a for air) and an energy balance ($m = e$):

$$\frac{\partial M_m}{\partial t} + \nabla \cdot Q_m = 0, \quad (A1)$$

where the mass accumulation terms (M_m with $m = w, t, a$) are given by

$$M_m = \phi(S_l \rho_l X_l^m + S_g \rho_g X_g^m) \quad (A2)$$

and the energy accumulation term (M_e) is given by

$$M_e = (1 - \phi)C_r T + \phi(S_l \rho_l u_l + S_g \rho_g u_g). \quad (A3)$$

The mass flux terms (Q_m with $m = w, t, a$) are given by the sum of the mass flux in each phase β (l for liquid and g for gas):

$$Q_m = Q_l^m + Q_g^m = -\frac{k k_{rl} \rho_l X_l^m}{\mu_l} (\nabla P_l - \rho_l g) - \frac{k k_{rg} \rho_g X_g^m}{\mu_g} (\nabla P_g - \rho_g g) + D_{va} \nabla X_g^m, \quad (A4)$$

and the energy flux term (Q_e) is given by

$$Q_e = -\lambda \nabla T + \sum_{\substack{\beta=l,g \\ m=w,t,a}} h_\beta^m Q_\beta^m. \quad (A5)$$

In the above equations, ϕ is porosity, S is saturation, ρ is density, X_β^m is the mass fraction of component m in phase β , C_r is rock volumetric heat capacity, T is temperature, u_β is the internal energy of the phase β , k is intrinsic permeability (in general, a tensor), $k_{r\beta}$ is the relative permeability of phase β , μ is viscosity, P is pressure, g is gravitational acceleration, D_{va} is the binary diffusion coefficient for water vapor and air, λ is thermal conductivity, and h_β^m is the enthalpy of component m in phase β . These equations are augmented by the closure conditions $S_l + S_g = 1$, $X_\beta^w + X_\beta^t + X_\beta^a = 1$ for each phase β , $P_g = P_v + P_a$, and $P_c = P_l - P_g$, where P_v and P_a are the partial pressures of water vapor and air, respectively, in the gas phase, and P_c is capillary pressure. The rock and all fluid phases are assumed to be in local thermodynamic equilibrium (i.e., within each grid block). TOUGH2 uses implicit time stepping and upstream weighting to determine interface properties.

Relative permeabilities and capillary pressure specified as functions of liquid saturation were developed to describe multiphase flow in porous media [Scheidtger, 1974], but in the past decade they have been widely applied to fractured rock [e.g., Pruess and Tsang, 1990; Reitsma and Kueper, 1994; Persoff and Pruess, 1995, and references therein]. The following functional forms are used in the present work (slightly more general versions may be found in the TOUGH user's guide [Pruess, 1987]). In the following expressions, the saturation S^* is defined as $S^* = (S_l - S_{lr})/(1 - S_{lr})$, where S_{lr} is the residual liquid saturation, defined as the saturation below which liquid is immobile (i.e., for $S^* \leq 0$, $k_{rl} = 0$, and $k_{rg} = 1$):

Corey [1954]

$$k_{rl} = S^{*4} \quad (A6)$$

$$k_{rg} = (1 - S^*)^2 (1 - S^{*2})$$

Power law

$$k_{rl} = S^{*4} \quad (A7)$$

$$k_{rg} = (1 - S^*)^n$$

van Genuchten [1980]

$$k_{rl} = S^{*1/2} [1 - (1 - S^{*1/m})^m]^2 \quad (A8)$$

$$k_{rg} = 1 - k_{rl}$$

$$P_c = -P_{c0} [S^{*-1/m} - 1]^{1-m} \quad S^* > 0, P_c < P_{cmax}$$

$$P_c = P_{cmax} \quad \text{otherwise.}$$

Acknowledgments. The careful review of this work by B. Faybishenko, S. Finsterle, K. Pruess, A. Simmons, and four anonymous reviewers is greatly appreciated. I have benefited from fruitful discussions throughout the course of these studies with Boris Faybishenko, Jane Long, and John Peterson. It has been a pleasure to use the elegant computer programs written by Karsten Pruess and Stefan Finsterle.

This work was supported by the Assistant Secretary for Environmental Restoration and Waste Management, EM-50, Office of Technology Development, Characterization, Monitoring and Sensor Technology Program, of the U.S. Department of Energy under contract DE-AC03-76SF00098.

References

- Baca, R. G., S. O. Magnuson, H. D. Nguyen, and P. Martian, A modeling study of water flow in the vadose zone beneath the Radioactive Waste Management Complex, *Rep. EGG-GEO-10068*, Idaho Natl. Eng. and Environ. Lab., Idaho Falls, 1992.
- Barenblatt, G. E., I. P. Zheltov, and I. N. Kochina, Basic concepts in the theory of homogeneous liquids in fissured rocks, *J. Appl. Math.*, 24(5), 1286–1303, 1960.
- Birkholzer, J., G. Li, C.-F. Tsang, and Y. W. Tsang, Modeling studies and analysis of seepage into drifts at Yucca Mountain, *J. Contam. Hydrol.*, 38, 349–384, 1999.
- Bishop, C. W., Hydraulic properties of vesicular basalt, M.Sc. thesis, Dep. of Hydrol. and Water Resour., Univ. of Arizona, Tucson, 1991.
- Corey, A. T., The interrelation between gas and oil relative permeabilities, *Prod. Mon.*, 19, 38–41, 1954.
- Doughty, C., Flow reduction due to degassing and redissolution phenomena, in *Proceedings of the TOUGH Workshop '95*, edited by K. Pruess, *Rep. LBL-37200*, pp. 227–232, E. O. Lawrence Berkeley Natl. Lab., Berkeley, Calif., 1995.
- Doughty, C., Investigation of conceptual and numerical approaches for evaluating gas, moisture, heat, and chemical transport in fractured unsaturated rock, *J. Contam. Hydrol.*, 38, 69–106, 1999a.
- Doughty, C., Mathematical modeling of a ponded infiltration test in unsaturated fractured basalt at Box Canyon, Idaho, *Rep. LBNL-40630*, E. O. Lawrence Berkeley Natl. Lab., Berkeley, Calif., 1999b.
- Faybishenko, B., Two field experiments for ponded infiltration in foundation pits, paper presented at AGU 13th Annual Hydrology Days, Colo. State Univ., Fort Collins, March 30 to April 2, 1993.
- Faybishenko, B. A., Hydraulic behavior of quasi-saturated soils in the presence of entrapped air: Laboratory experiments, *Water Resour. Res.*, 31(10), 2421–2435, 1995.
- Faybishenko, B., et al., Ponded infiltration test at the Box Canyon site: data report and preliminary analysis, *Rep. LBNL-40183*, E. O. Lawrence Berkeley Natl. Lab., Berkeley, Calif., 1997.
- Faybishenko, B., P. Holland, M. Mesa, D. Burgess, C. F. Knutson, and J. B. Sisson, Lithological conditions at the Box Canyon site: Results of drilling, coring, and open borehole measurements, 1995–1997 data report, *Rep. LBNL-40182*, E. O. Lawrence Berkeley Natl. Lab., Berkeley, Calif., 1998.
- Faybishenko, B., C. Doughty, M. Steiger, J. C. S. Long, T. R. Wood, J. S. Jacobsen, J. Lore, and P. T. Zawislanski, Conceptual model of the geometry and physics of water flow in a fractured basalt vadose zone, *Water Resour. Res.*, this issue.
- Knutson, C. F., K. A. McCormick, J. C. Crocker, M. A. Glenn, and M. L. Fishel, 3D RWC vadose zone modeling, *Rep. EGG-ERD-10246*, Idaho Natl. Eng. and Environ. Lab., Idaho Falls, 1992.
- Liou, T.-S., K. Pruess, and Y. Rubin, Numerical simulation of experiments on water seepage in unsaturated, heterogeneous fractures, in *Proceedings of the TOUGH Workshop '98*, edited by K. Pruess, *Rep. LBNL-41995*, pp. 198–204, E. O. Lawrence Berkeley Natl. Lab., Berkeley, Calif., 1998.
- Long, J. C. S., et al., Analog site for fractured rock characterization, annual report FY 1995, *Rep. LBL-38095*, E. O. Lawrence Berkeley Natl. Lab., Berkeley, Calif., 1995.
- Magnuson, S. O., Inverse modeling for field-scale hydrologic and transport parameters of fractured basalt, *Rep. INEL-95/0637*, Idaho Natl. Eng. and Environ. Lab., Idaho Falls, 1995.
- Moridis, G., and K. Pruess, TOUGH simulations of Updegraff's set of fluid and heat flow problems, *Rep. LBL-32611*, E. O. Lawrence Berkeley Natl. Lab., Berkeley, Calif., 1992.
- Moridis, G., and K. Pruess, Flow and transport simulations using T2CG1, a package of conjugate gradient solvers for the TOUGH2 family of codes, *Rep. LBL-36235*, E. O. Lawrence Berkeley Natl. Lab., Berkeley, Calif., 1995.
- National Research Council Committee on Fracture Characterization and Fluid Flow, *Rock Fractures and Fluid Flow: Contemporary Understanding and Applications*, Chapter 6, Natl. Acad. Press, Washington, D. C., 1996.
- Persoff, P., and K. Pruess, Two-phase flow visualization and relative permeability measurement in natural rough-walled rock fractures, *Water Resour. Res.*, 31(5), 1175–1186, 1995.
- Peterson, J. E., Jr., and K. H. Williams, Ground penetrating radar results at the Box Canyon site: 1996 survey as part of infiltration test, *Rep. LBNL-40915*, E. O. Lawrence Berkeley Natl. Lab., Berkeley, Calif., 1997.
- Philip, J. R., Numerical solution of equations of the diffusive type with diffusivity concentration dependent, *Trans. Faraday Soc.*, 51, 885–892, 1955.
- Pruess, K., TOUGH user's guide, *Rep. LBL-20700*, E. O. Lawrence Berkeley Natl. Lab., Berkeley, Calif., 1987.
- Pruess, K., TOUGH2—A general-purpose numerical simulator for multiphase fluid and heat flow, *Rep. LBL-29400*, E. O. Lawrence Berkeley Natl. Lab., Berkeley, Calif., 1991.
- Pruess, K. (Ed.), *Proceedings of the TOUGH Workshop '95*, *Rep. LBL-37200*, E. O. Lawrence Berkeley Natl. Lab., Berkeley, Calif., 1995.
- Pruess, K. (Ed.), *Proceedings of the TOUGH Workshop '98*, *Rep. LBNL-41995*, E. O. Lawrence Berkeley Natl. Lab., Berkeley, Calif., 1998.
- Pruess, K., and Y. W. Tsang, On two-phase relative permeability and capillary pressure of rough-walled rock fractures, *Water Resour. Res.*, 26(9), 1915–1926, 1990.
- Pruess, K., J. S. Y. Wang, and Y. W. Tsang, On thermohydrologic conditions near high-level nuclear wastes emplaced in partially saturated fractured tuff, 1, Simulation studies with explicit consideration of fracture effects, *Water Resour. Res.*, 26(6), 1235–1248, 1990a.
- Pruess, K., J. S. Y. Wang, and Y. W. Tsang, On thermohydrologic conditions near high-level nuclear wastes emplaced in partially saturated fractured tuff, 2, Effective continuum approximation, *Water Resour. Res.*, 26(6), 1249–1261, 1990b.
- Rawson, S. A., J. C. Walton, and R. G. Baca, Modeling potential migration of petroleum hydrocarbons from a mixed-waste disposal site in the vadose zone, paper presented at Petroleum Hydrocarbons and Organic Chemicals in Groundwater: Prevention, Detection, and Restoration, Natl. Water Well Assoc., Houston, Tex., Nov. 15–17, 1989.
- Reitsma, S., and B. H. Kueper, Laboratory measurement of capillary pressure-saturation relationships in a rock fracture, *Water Resour. Res.*, 30(4), 865–878, 1994.
- Salve, R., C. Doughty, J. P. Fairley, P. J. Cook, and J. S. Y. Wang, Fracture/matrix test in Alcove 6, in *Progress Report on Fracture Flow, Drift Seepage and Matrix Imbibition Tests in the Exploratory Studies Facilities*, edited by J. S. Y. Wang et al., *Spec. Publ. SP33PBM4*, pp. 3.1–3.95, Yucca Mt. Proj. Milestone, E. O. Lawrence Berkeley Natl. Lab., Berkeley, Calif., 1998.
- Sawada, A., M. Shiotsuki, K. Oyamada, and H. Takase, Study of flow model comparison in fractured rock, *Proc. Int. Symp. Rock Mech.*, 30th, 123–127, 1999.
- Scheidegger, A. E., *The Physics of Flow Through Porous Media*, 3rd ed., Univ. of Toronto Press, Toronto, Ont., 1947.
- van Genuchten, M. T., A closed-form equation for predicting the hydraulic conductivity of unsaturated soils, *Soil Sci. Soc. Am. J.*, 44, 892–898, 1980.
- Vauclin, M., D. Khanji, and G. Vachaud, Experimental and numerical study of a transient, two-dimensional unsaturated-saturated water table recharge problem, *Water Resour. Res.*, 15(5), 1089–1101, 1979.
- Warren, J. E., and P. J. Root, The behavior of naturally fractured reservoirs, *Soc. Pet. Eng. J.*, 228, 245–255, 1963.
- Wood, T. R., and G. T. Norrell, Integrated large-scale aquifer pumping and infiltration tests: Groundwater pathways OU 7-06: Summary report, *Rep. INEL-96/0256*, Idaho Natl. Eng. and Environ. Lab., Idaho Falls, 1996.

C. Doughty, Earth Sciences Division, E. O. Lawrence Berkeley National Laboratory, 1 Cyclotron Road, MS 90-1116, University of California, Berkeley, CA 94720. (cadoughty@lbl.gov)

(Received March 9, 1999; revised May 5, 2000; accepted May 10, 2000.)